Nano Energy, Volume 47, May 2018, Pages 285-293
DOI: 10.1016/j.nanoen.2018.03.003

Thermal strain induced large electrocaloric effect of relaxor thin film on LaNiO3/Pt composite electrode with the coexistence of nanoscale antiferroelectric and ferroelectric phases in a broad temperature range

Biaolin Peng[1,2,3], Qi Zhang[3], Yinong Lyu[2], Laijun Liu[2], Xiaojie Lou[4], Christopher Shaw[3], Haitao Huang[2]*, Zhonglin Wang[5]*

[1]Guangxi Key Laboratory for Relativistic Astrophysics, School of Physical Science & Technology, Guangxi University, Nanning 530004, China

[2]Department of Applied Physics, The Hong Kong Polytechnic University, Kowloon, Hong Kong SAR

[3]School of Aerospace, Transport and Manufacturing, Cranfield University, Cranfield, Bedfordshire, MK43 0AL, United Kingdom

[4]Frontier Institute of Science and Technology, State Key Laboratory for Mechanical Behavior of Materials, MOE Key Laboratory for Nonequilibrium Synthesis and Modulation of Condensed Matter, Xi'an Jiaotong University, Xi'an 710049, China

[5]School of Materials Science and Engineering，Georgia Institute of Technology，Atlanta, GA 30332-0245, USA

*Correspondence to: aphhuang@polyu.edu.hk, zhong.wang@mse.gatech.edu

Abstract: Ferroelectric/antiferroelectric thin/thick films with large electrocaloric (EC) effect in a broad operational temperature range are very attractive in solid-state cooling devices. We demonstrated that a large positive electrocaloric (*EC*) effect (maximum $\Delta T \sim 20.7$ K) in a broad temperature range (~ 110 K) was realized in $Pb_{0.97}La_{0.02}(Zr_{0.65}Sn_{0.3}Ti_{0.05})O_3$ (PLZST) relaxor antiferroelectric (AFE) thin film prepared using a sol-gel method. The large positive *EC* effect may be ascribed to the in-plane residual thermal tensile stress during the layer-by-layer annealing process, and the high-quality film structure owing to the utilization of the $LaNiO_3$/Pt composite bottom electrode. The broad *EC* temperature range may be ascribed to the great dielectric relaxor dispersion around the dielectric peak because of the coexistence of nanoscale multiple FE and AFE phases. Moreover, a large pyroelectric energy density (6.10 Jcm^{-3}) was harvested by using an Olsen cycle, which is much larger than those (usually less than $10^{-4}Jcm^{-3}$) obtained by using direct thermal-electrical, Stirling and Carnot cycles, etc. These breakthroughs enable the PLZST thin film an attractive multifunctional material for applications in modern solid-state cooling and energy harvesting.

Keywords: electrocaloric; antiferroelectric; relaxor; thin film; sol-gel

1. Introduction

Recently, more and more research attentions have been drawn to the electrocaloric (EC) refrigeration based on the EC effect in ferroelectric/antiferroelectric (FE/AFE) thin/thick films [1-4], which is regarded as a potential competitive solid-state refrigeration technology with wide applications in electronic devices such as computers and cell phone [5-10], etc. EC effect is represented by an induced change in the adiabatic temperature (ΔT) or isothermal entropy (ΔS) of a polarizable dielectric material upon the application or withdrawal of an electric field [2, 3, 11]. Compared to the rapid development of magnetic refrigeration based on the magnetocaloric (MC) effect [1, 12], EC refrigeration is hardly progressed at all for a long time in the past since only a small ΔT (2.5 K) and ΔS (0.2 $JK^{-1}kg^{-1}$) can be observed [13] due to the restriction of low dielectric breakdown strength (usually less than 100 $kVcm^{-1}$) in bulk ceramics. However, EC refrigeration has the potential to be a more viable candidate as electric fields are easier to achieve and contemporary known magnetocaloric materials require substantial magnetic fields (>1 T) to operate [14].

In 2006, Mischenko *et al*. reported a giant EC effect (ΔT = 12 K and ΔS = 8 J $K^{-1}kg^{-1}$) in the AFE $PbZr_{0.95}Ti_{0.05}O_3$ (PZT) thin film [3], which is near the AFE to paraelectric (PE) phase transition temperature (T_C = 500 K). Triggered by Mischenko's research work, a lot of theoretical and experimental studies in various FE/AFE bulk and film systems have been conducted and have revealed the existence of two EC effects, i.e., the normal (positive) ($\Delta T > 0$) and anomalous effects (negative) ($\Delta T < 0$). For positive EC effect, it is generally believed that large ΔT can be obtained near the Curie temperature (*Tc*), as reported by Mischenko *et al*. However, large positive EC effect can also be achieved at a AFE/FE phase transition temperature rather than near the T_C, such as large $\Delta T \sim$ 45.3 K at 17 °C and 598 $kVcm^{-1}$ in $Pb_{0.8}Ba_{0.2}ZrO_3$ thin film (320 nm in thickness) [11], and 53.8 K at 5 °C in $Pb_{0.97}La(Zr_{0.75}Sn_{0.18}Ti_{0.07})O_3$ thick film (2 μm in thickness) [4], etc. Compared to the large ΔT values obtained in the positive EC effect, the absolute value of the ΔT observed in negative *EC* effect is smaller, such as $\Delta T \sim$ - 5.76 K at 59 °C and 338 $kVcm^{-1}$ in $Pb_{0.97}La_{0.02}(Zr_{0.95}Ti_{0.05})O_3$ thin film (650 nm thickness) [15], $\Delta T \sim$ - 6.62 K at 130 °C and 709 $kVcm^{-1}$ in $Pb_{0.96}Eu_{0.04}ZrO_3$ thin film (550

nm thickness) [16], and ΔT ~ - 10.8 K at 175 °C and 3260 kVcm^{-1} in $Hf_{0.5}Zr_{0.5}O_2$ thin film (9.2 nm thickness) [17], etc. Usually, the origin of a negative EC effect can be traced to the non-collinearity between the electric field and the polarization [15, 18-21]. Researchers also believe that a high cooling efficiency can be achieved upon the combination of the positive and negative EC effects. For example, Li et al. suggested that the 180° domain structure of $PbTiO_3$ can be utilized as a combined nano-laminate structure to include positive and negative EC materials [22]. As a result, the combination of positive and negative EC effects in thin films can complete the cooling process in one step with a sustained applied electric field in the cooling process [17, 23], leading to a high cooling efficiency.

However, in addition to the required large ΔT value and high cooling efficiency in positive/negative EC effects, a broad operational temperature range is also required for practical commercial application in cooling devices. Although the maximum ΔT value in EC effect is large, the operational temperature range is usually narrow, such as the full width at half maximum value of ΔT ($FWHM_{\Delta T}$) ~ 10 K in the $Pb_{0.8}Ba_{0.2}ZrO_3$ thin films [11], and the $FWHM_{\Delta T}$ ~ 25 K in the $Pb_{0.97}La(Zr_{0.75}Sn_{0.18}Ti_{0.07})O_3$ thin films [4]. The refrigeration industry would require the $FWHM_{\Delta T}$ to span over more than 50 K, which is unlikely to ever be achieved in classical ferroelectrics [24].

In this work, we report a large positive electrocaloric (*EC*) effect (the maximum ΔT ~ 20.7 K) in a broad temperature range ($FWHM_{\Delta T}$ ~ 110 K) in relaxor $Pb_{0.97}La_{0.02}(Zr_{0.65}Sn_{0.3}Ti_{0.05})O_3$ (PLZST) thin film deposited on a $LaNiO_3$/Pt composite bottom electrode. The composition of PLZST thin film is designed to locate at a morphotropic phase boundary (MPB) with a coexistence of nanoscale tetragonal AFE and orthorhombic AFE phases [25], as shown in **Fig. 1a)**. The large ΔT and $FWHM_{\Delta T}$ are attributed to the in-plane residual thermal tensile stress produced during the layer-by-layer annealing process and the great dielectric relaxor dispersion around the dielectric peak because of the coexistence of nanoscale multiple FE and AFE high temperature phases, respectively. Moreover, a large pyroelectric energy density (6.10 Jcm^{-3}) is also harvested by using an

Olsen cycle. These breakthroughs make the materials very attractive for practical applications in cooling devices and other multifunctional devices.

2. Materials and Methods

2.1. Fabrication of PLZST: PLZST thin films were prepared by using a sol-gel method as shown in **Fig. S1a)**. $Pb(CH_3COO)_2$ with 20% excess Pb, $Sn(CH_3COO)_4$ and $La(OC_2H_5)_3$ were dissolved in 110 °C glacial acetic acid. Simultaneously, $Zr(OC_3H_7)_4$ and $Ti(OCH(CH_3)_2)_4$ were dissolved in a mixture of glacial acetic and $CH_3COCH_2COCH_3$ at room temperature. The Pb/Sn/La and Zr/Ti solutions were then mixed and stirred for 30 min at 80 °C. After that, appropriate additives (lactic acid, 1-propyl alcohol and water) were added into the mixed Pb/Sn/La/Zr/Ti solution. The final concentration of the PLZST precursor solution was 0.3 M. After the precursor solution was aged for 24 h, the PLZST thin films were deposited on several different bottom electrodes that were rinsed with acetone and ethanol. These electrodes include $Pt(111)/TiO_x/SiO_2/Si(100)$ (abbreviated as Pt) electrode, $LaNiO_3/Pt(111)/TiO_x/SiO_2/Si(100)$ (abbreviated as $LaNiO_3$/Pt) composite electrode and $LaNiO_3/Si(100)$ (abbreviated as $LaNiO_3$) electrode. The PLZST thin films were prepared by layer-by-layer (A-type) and multiple layer (B-type) annealing modes, respectively. For the A-type mode (see the route guided by the red arrows in Fig.S1a), each layer of film was spin-coated at 5000 rpm for 30 s. Every wet film was first dried at 150 °C for 3 min and then pyrolyzed at 450 °C for 3 min on hotplates, and finally was annealed in a tube furnace at 700 °C for 3 min in air. The above process was repeated for 8 times. In B-type mode (see the route guided by the blue arrows in Fig.S1a), the coating, drying and pyrolyzing process were repeated for 8 times first. Then the PLZST thin film was obtained by annealing at 700 °C for 30 min (rather than 3 min) to ensure full crystallization. The final film thickness was about 420 to 480 nm, depending on the types of bottom electrodes and the annealing mode of deposition.

2.2. Fabrication of $LaNiO_3$/Pt and $LaNiO_3$/Si bottom electrodes: $LaNiO_3$/Pt and $LaNiO_3$/Si bottom electrodes were prepared by using a sol-gel method as shown in **Fig. S1b)**. $Ni(CH_3COO)_2$ and $La(NO_3)_3$ were dissolved in a mixture of glacial acetic acid, water and formamide (CH_3NO) at room

temperature. The final concentration of the $LaNiO_3$ precursor solution was 0.3 M. After the precursor solution was aged for 24 h, $LaNiO_3$ thin film with 6 layers was deposited on Pt(111)/TiO_x/SiO_2/Si(100) and Si(100) substrates by using A-type annealing mode.

2.3. Characterization: The crystallinity of the PLZST thin film was monitored by X-ray diffraction (XRD; Rigaku 9 KW Smartlab, Tokyo, Japan). The cross-sectional morphology of the film was examined by scanning electron microscopy (SEM, FEI Sirion 200). The microstructure of the film was studied by transmission electron microscopy (TEM; JEOL JEM-2100F). For measurement of the electrical properties, Au/Cr top electrodes with a diameter of 150 μm (**Fig. S2**) were deposited by RF magnetron sputtering using a shadow mask. Dielectric permittivity measurement was carried out using an impedance analyzer (E4980A, Agilent) with a perturbation voltage Vac = 100 mV. Polarization-electric field ($P-E$) hysteresis loops were obtained by means of a ferroelectric tester (Precision Premier II, Radiant Technologies Inc., Alpharetta, GA). Electrical resistivity of bottom electrode was measured by a four-point-probe meter. All samples were measured with top-to-bottom electrode configuration. The temperature of the sample was controlled by a thermal controller (THMSG600, Linkam) with an accuracy of 0.1°C.

3. Results

3.1. Structure

X-ray diffraction (XRD) patterns of $Pb_{0.97}La_{0.02}(Zr_{0.65}Sn_{0.3}Ti_{0.05})O_3$ (PLZST) thin films at a morphotropic phase boundary (MPB) with the coexistence of AFE_T and AFE_O (red dots in **Fig. 1a**) are shown in **Fig. 1b)**. All thin films exhibit good crystallinity and pure perovskite phase. For simplicity, the diffraction peaks are indexed using the pseudo-cubic structure rather than the orthorhombic or tetragonal one. The film deposited on Pt bottom electrode with A-type annealing mode exhibits a weak (100)-preferred orientation (black curve). In addition to the (100)-preferred peak, the (111) peak can also be observed, which is broadened and split into two obvious peaks (O(042/202) and O(230/212)) (see black arrows), indicating the existence of the orthorhombic AFE phase. The thin film deposited on $LaNiO_3$ bottom electrode with A-type annealing mode

exhibits a strong (100)-preferred orientation (red curve). The (200) peak is broadened and split into two visible peaks (T(002) and T(200)) (the ratio of c/a ~ 1.03), indicating the existence of the tetragonal AFE phase. The thin film deposited on $LaNiO_3$/Pt composite bottom electrode with A-type annealing modes exhibits a strong (100)-preferred orientation (blue curve) with a weak partner of (111) peak. Different to the (100)-preferred orientation in those thin films with A-type annealing modes, the thin film deposited on $LaNiO_3$/Pt composite bottom electrode with B-type annealing mode exhibits a random orientation (green curve). The above results show that the composition of PLZST thin film is indeed located at the MPB with a coexistence of AFE_T and AFE_O [25].

The cross-sectional SEM of the thin film deposited on the Pt bottom electrode with A-type annealing mode shows disordered growth of nanocrystals (**Fig. 2a)**). Columnar-like texture which usually will appears in lead-based thin films deposited on Pt/TiOx/SiO_2/Si substrate with the layer-by-layer annealing mode [26] cannot be observed. Instead, a large number of micro cracks are visible on the corresponding film surface (**Fig. 2b)**) because of the poor adhesion of the Pt electrode to the TiOx/SiO_2/Si substrate at high temperature (> 650 °C). Also a large number of hillocks generated by the compressive stress [27] can also be detected (**Fig. S2a)**). The emerging of hillocks usually cause large leakage current, resulting in a deterioration of the performance of the thin film capacitor, especially at operating conditions of high temperature and high electric field. Compared with the disordered growth of nanocrystals in the thin film deposited on the Pt electrode, a highly (100)-preferred ordered columnar-like texture is visible (**Fig. 2c)**) for the thin film deposited on the $LaNiO_3$ electrode with A-type annealing mode. No obvious micro cracks except some ultra-fine cracks can be observed on the surface (**Fig. 2d)**). A highly ordered columnar-like texture can also be obtained (**Fig. 2e)**) for the thin film deposited on the $LaNiO_3$/Pt composite electrode with A-type annealing mode. Particularly, crack-free surface **(Fig. 2f))** bearing an embryo rosette structure [11, 28] can be observed, which indicated that the $LaNiO_3$/Pt composite electrode is beneficial to obtain crack-free structure. However, only a random ordered rosette structure [11, 28] is obtained in the thin film deposited on the $LaNiO_3$/Pt composite electrode with B-

type annealing mode (**Fig. 2g) and 2h)**). It should be noted that the surface color filtered optical microscope images of the top electrodes, no matter in the film deposited on $LaNiO_3$ electrode or in those deposited on $LaNiO_3$/Pt composite electrode with A-type or B-type annealing modes, all images look smooth and clear as shown in **Fig. S2b)** rather than rough and fuzzy as shown in **Fig. S2a),** where the film is deposited on Pt bottom electrode directly. It reveals that the utilization of $LaNiO_3$ oxide conductive layer can help inhibit the formation of hillocks.

Fig. 3a) shows the cross-sectional TEM image of the PLZST thin film deposited on the $LaNiO_3$/Pt composite electrode with A-type annealing mode. It can be found that the PLZST thin film with a thickness of about 430 nm is uniform, homogeneous, and crack-free. Nanocrystals with an average grain size of 10 nm are clearly visible in an enlarged image (inset of **Fig. 3a)**). Inside of some nanocrystals, lamellar nanodomains with ~ 1 nm width (the red dotted circle) can be observed. **Fig. 3b)** shows the corresponding cross-sectional high-resolution transmission electron microscope (HRTEM) image of the enlarged part of the thin film. Two adjacent laminar domains are clearly visible, as marked by the letters A and B. The Fourier transform patterns of the HRTEM image of the two adjacent laminar domains are shown in the inset of **Fig. 3b).** It can be found that each of the fundamental reflections is satellited by two superlattice reflections (the blue or red dots in pairs) with diffused steaks, indicating the existence of the incommensurately modulated polar structures [25]**.** These incommensurate modulated polar structures are believed to originate from the competition between antiferroelectric and ferroelectric coupling [25], and such interaction can be strengthened by doping of La. They often play an important role in the electric and mechanical properties of materials.

3.2. Dielectric properties

Fig. 4 shows the temperature dependence of the relative dielectric permittivity ($\varepsilon(T)$) and the dielectric loss (tan $\delta(T)$) of PLZST thin films. The thin film deposited on the Pt electrode with A-type annealing mode exhibits the highest value of dielectric permittivity ($\varepsilon \approx 465$) with a moderate value of dielectric loss (tan $\delta \approx$ 0.023) at room temperature (**Fig. 4a)**). By contrast, the thin film deposited on the $LaNiO_3$ electrode with A-

type annealing mode exhibits the highest value of dielectric loss (tan δ ≈ 0.052) with a moderate value of dielectric permittivity ($\varepsilon \approx 391$) (**Fig. 4b)**). By using the $LaNiO_3$/Pt composite electrode, the thin film with A-type annealing mode exhibits a moderate value of dielectric permittivity ($\varepsilon \approx 423$) with a moderate value of dielectric loss (tan δ ≈ 0.026) (**Fig. 4c)**). In view of the XRD analysis, the difference in dielectric permittivity among these thin films may be resulted from their different spontaneous polarization directions ([110] and [001] for AFE_O and AFE_T phases, respectively). The thin film deposited on the $LaNiO_3$/Pt composite electrode with B-type annealing mode exhibits both the lowest value of dielectric permittivity ($\varepsilon \approx 226$) and the lowest value of dielectric loss (tan δ ≈ 0.019) (**Fig. 4d)**). Differences in dielectric properties between the A-type and B-type thin films are possibly ascribed to their preferred orientations and the phase structures which will be discussed later. It can be seen that all thin films exhibit prototypical relaxor characteristics, namely, both the temperature (T_m) of dielectric permittivity maximum and the temperature (T_m^{δ}) of maximum dielectric loss shift towards higher temperature with increasing frequency [29, 30]. Meanwhile, dielectric dispersion appears around the T_m, whereas the maximum values of dielectric loss increases with increasing frequency. The dielectric relaxation behavior of thin films around the T_m can be well described by the Lorentz-type empirical relation, $\varepsilon_A/\varepsilon=1+(T-T_A)^2/2\delta_A{}^2$ [31, 32], as shown by the colored dotted lines in **Fig. 4a)** to **4d)**. The parameter δ_A reflects the relaxor diffuseness of the dielectric peak. The greater the relaxor dispersion, the larger the δ_A. The Lorentz fitting parameters δ_A around T_m (at 10 kHz) for the thin films deposited on the Pt, $LaNiO_3$, and $LaNiO_3$/Pt composite electrodes with the A-type annealing mode are 107.9, 143.1 and 120.2 respectively. It is found that the δ_A of thin films are negatively linked to their electrical conductivity ($\sigma_{electric}^{LaNiO_3,119\Omega} < \sigma_{electric}^{LaNiO_3/Pt,5.0\Omega} < \sigma_{electric}^{Pt,1.5\Omega}$) by comparison with the electrical resistivity chart (**Fig. S3d)**) of the bottom electrodes. The smaller the electrical conductivity is, the larger the δ_A is. It has been well known that the electrical conductivity of the $LaNiO_3$ oxide electrode tends to decrease with increasing temperature and the Ohm contact between the bottom electrode and the thin film will get worse. Therefore, it can be inferred that the worse Ohm contact may be responsible for the large relaxor dispersion of the thin film deposited on the $LaNiO_3$

electrode, and also the large frequency dispersion of the dielectric permittivity (ε_{10kHz}-ε_{1MHz}), as well as the upward shift of the permittivity on the high temperature side of the weak dielectric peak, as shown in **Fig. 4b)**. The δ_A of the thin film deposited on the $LaNiO_3$/Pt composite electrode with the B-type annealing mode is only 101.1, which is smaller than that (120.2) of the A-type thin film. The smaller δ_A in the B-type thin film may be ascribed to its random orientation and the unique phase structure (coexistence of AFE and FE phases induced by thermal stress during the process of deposition). Detailed discussion about the phase structure will be available in the subsequent parts of this article. The deviations between experimental and theoretical values (Lorentz extrapolation) on the low-temperature sides of all dielectric peaks may be attributed to the coexistence of AFE_T and AFE_O phases in PLZST thin films, similar to the case of $(Pb_{0.8}Ba_{0.2})ZrO_3$ thin films [26]. The coexisted AFE_T and AFE_O phases in the PLZST thin films at room temperature transform gradually into the FE_R phase with increasing temperature (**Fig. S4** and **Fig.1a)**), and finally evolved into Pseudo-cubic or cubic phases. As a result, the AFE_T, AFE_O and FE_R phases are believed to coexist around the diffused dielectric peak. The coexistence of multiple phases may be responsible for the large relaxor dispersion in the PLZST thin films.

3.3. Electrocaloric effect

To assess the *EC* effect in PLZST thin films, the *P*-*E* loops at 10 kHz were measured at a step of ten degrees in the temperature range between 20 and 270 °C. To avoid dielectric breakdown, a safety electric field playing an important role in obtaining a large ΔT is applied [33, 34], which is far below the mean dielectric breakdown strength (DBS) estimated by the Weibull distribution, as shown in **Fig. S5**. For example, the DBS of the thin film deposited on the $LaNiO_3$/Pt composite electrodes with the A-type annealing mode is about 2436 $kVcm^{-1}$, much higher than 1092 $kVcm^{-1}$ (the safety electric field applied). Representative *P*-*E* loops are shown in **Fig. 5a)**, **5c)**, **5)** and **5g)**. It is noted that the polarizations of the thin films are related to the films' orientations depended on the types of the bottom electrodes and the annealing modes. The temperature dependences of the polarizations ($P(T)$) at selected electric fields were extracted from the upper branches of

the *P*-*E* loops in $E > 0$ and presented in the upper left insets of **Fig. 5a)**, **5c)**, **5e)** and **5g)**. The color solid lines in these insets represent cubic-spline interpolations of the raw experimental data. The curves of pyroelectric coefficients versus temperature ($(\partial P/\partial T)_E(T)$) at selected electric field were derived from the differential values of $P(T)$ curves and plotted in the lower right insets of **Fig. 5a)**, **5c)**, **5e)** and **5g)**.

Based on the Maxwell relationship $(\partial S / \partial E)_T = (\partial P / \partial T)_E$, reversible adiabatic changes in temperature (ΔT) and entropy (ΔS) of a dielectric material can be determined by [2, 3, 11]:

$$\Delta T = -\frac{1}{\rho}\int_{E_1}^{E_2} \frac{T}{C}\left(\frac{\partial P}{\partial T}\right)_E dE \tag{1}$$

$$\Delta S = -\frac{1}{\rho}\int_{E_1}^{E_2} \left(\frac{\partial P}{\partial T}\right)_E dE \tag{2}$$

where T is the operation temperature, P is the maximum polarization at the applied electric field E, ρ is the density, C is the heat capacity that is assumed to be constant in the whole temperature range studied, and E_1 and E_2 are the initial and final applied electric fields, respectively. The ρ (calculated from the XRD) and C in the temperature range studied are 8.7 gcm^{-3} and 0.33 $JK^{-1}g^{-1}$ [4], respectively. The adiabatic temperature change ΔT and entropy change ΔS of PLZST thin films are plotted in **Fig. 5b), 5d), 5f), and 5h)**. It can be seen that two fake negative *ECs* were observed in thin films deposited on the Pt and $LaNiO_3$ electrodes around their dielectric peaks. The ΔT for the two thin films at 1092 kV/cm are - 7.7 and - 6.8 K, respectively, and the corresponding ΔS are - 4.8 and - 4.2 $JK^{-1}Kg^{-1}$, respectively. It has been well known that defects (cracks and hillocks, etc.) in thin films may cause a large leakage current, especially at high temperature and high electric field. Therefore, based on the analysis results of the **Fig. 2**, **Fig. S2**, and **Fig. S3**, it can be inferred that the fake negative *EC* in thin film deposited on the Pt electrode may be ascribed to the surface micro cracks and the hillocks, and the fake negative *EC* in thin film deposited on the $LaNiO_3$ electrode may be related to the surface ultra-fine cracks and the low electrical conductivity of the $LaNiO_3$ electrode. In contrast with the two fake negative *ECs*, a large positive *EC* ($\Delta T > 10$K) in a broad temperature range (about 110 K) was achieved in thin film deposited on the $LaNiO_3$/Pt composite electrode with A-type annealing mode around its dielectric

peak, as marked by the green vertical lines in **Fig. 5f)**. The maximum ΔT which is located at the left side of the dielectric peak T_m is about 20.7 K at 192 °C, and the corresponding ΔS is about 14.7 $JK^{-1}Kg^{-1}$. In addition to the large positive *EC* around the dielectric peak, a small intrinsic negative *EC* (ΔT ~ 1 K) in a broad temperature range (from 20 °C to 150 °C) can also be observed at a moderate electric field (143 $kVcm^{-1}$), as marked by the black vertical lines in **Fig. 5f)**. With a further increase of the applied electric field, the small negative *EC* transferred into a positive *EC*, indicating an occurrence of field-induced phase transition (AFE to FE). According to previous research work [15, 19, 20], the origin of the small negative *EC* may be ascribed to some factors such as the noncollinearity between polarization and electric field, the subtle coupling between AFEs, induced FEs and oxygen octahedron tilting instabilities, and so on. Compared with the large positive *EC* in the A-type thin film, the positive *EC* in B-type thin film is small, as marked by the green vertical lines in **Fig. 5h)**. The maximum ΔT is only about 6.4 K at 198 °C, and the corresponding ΔS is only about 4.5 $JK^{-1}Kg^{-1}$. Moreover, the weak negative *EC* near the room temperature is almost invisible, and the absolute value (< 0.1 K) of ΔT is far below that (~ 1 K) of the A-type thin film, indicating that there is a small amount of AFE phases existing in the B-type thin film, as shown by the low current peaks (1 & 3) in **Fig. S6h)**.

3.4. Energy harvesting performance

The energy harvesting of the PLZST thin film can be realized by using an Olsen cycle [35], as schematically guided by the red arrows in **Fig. 6**. Process 1 → 2 is an isothermal increase of the electric field at low temperature (T_L). Process 2 → 3 is the heating of the thin film from T_L to high temperature (T_H) at high electric field (E_H). Process 3 → 4 is an isothermal decrease of the electric field at T_H. Process 4 → 1 is the cooling of the material at low electric field (E_L), which completes one cycle. The harvested pyroelectric energy density in a closed cycle is equal to the area of the cycle 1 → 2 → 3 → 4, and can be expressed as [35-40],

$$W = \oint EdP \tag{3}$$

where E is the electric field, and P is the polarization. The maximum harvested pyroelectric energy density between the T_L (20 °C) and T_H (260 °C) for the A-type thin film deposited on the $LaNiO_3$/Pt composite

electrode is 6.10 Jcm^{-3}, which is about 7.3 times larger than that (0.84 Jcm^{-3}) of the B-type thin film, and much larger than those (usually less than $10^{-2}Jcm^{-3}$) harvested by using direct thermal-electrical cycle, Stirling cycle or Carnot cycle [41]. It should be pointed out that 6.10 Jcm^{-3} is only an ideal value. Some W_{losses} should be included. The W_{losses} is the sum of a variety of energy losses (per cycle including hysteresis and conduction loss in the pyroelectric material and control and pumping and other losses in the system)[41].

4. Discussion

To gain insight into the effect of annealing mode on the *EC* performance of the PLZST thin films, two schematic models about the relationship between the thermal stress and phase structure are proposed, as shown by the upper right insets in **Fig. 5f)** and **5h)**. Due to the lower thermal expansion coefficients (α) of the Si substrate (α_{sub} ~ 0.2 - 0.5 $\times 10^{-6}$ K^{-1} from room temperature to 700 °C) than that of the PLZST thin film (α_f ~ 0.5 ~ 2 $\times 10^{-5}$ K^{-1}) [42, 43], in the A-type annealing mode, an in-plane tensile stress in the thin film was developed during cooling down of the film after its fully crystallization at the annealing temperature [44]. For the PLZST thin films with the A-type annealing mode, the tensile stress was established in each PLZST layer during repeated annealing processes (crystallization at high temperature and cooling down) [44] (see the upper right inset in **Fig. 5f**), which can be estimated to be ~ 500 MPa according to the formula:$\sigma = \int_{RT}^{T_{ann}} \frac{Y}{1-v} \times (\alpha_f(T) - \alpha_{sub}(T))dT$, where $\alpha_f(T)$ and $\alpha_{sub}(T)$ are the temperature dependence of the thermal expansion coefficient (α_f ~ 5.4 × 10^{-6} K^{-1}) of the PLZST films and the Si substrate (α_{sub} ~ 3.6 × 10^{-6} K^{-1}), respectively, and Y Young's modulus and v Poisson's ratio of the films [45]. Accordingly, the AFE phases (see the double *P-E* loops in **Fig. 5a)**, **5c)** and **5e**) will be well kept since the in-plane tensile stress is helpful to stabilize them in the PLZST thin films [46]. It should be noted that the residual stress also depends on the film orientation due to the anisotropic thermal expansion of the PLZST thin film [44]. Stress relaxation however, depends on the film microstructure. Different to the uniform distribution of the in-plane residual tensile thermal stress in the A-type annealing process (the upper right inset in **Fig. 5f**), a gradient distribution of the in-plane residual tensile thermal stress (the upper right inset in **Fig. 5h**) was developed in the B-type annealing process. The in-

plane residual tensile thermal stress was well kept in the first layer which is adjacent to the substrate. However, the in-plane residual tensile stress was released gradually as the number of the layers increases. Accordingly, only those AFE phases in the first layer were well preserved, and the AFE phases in those layers which were far away from the substrate were gradually transformed into FE phases due to the degradation or relaxation of the in-plane residual tensile thermal stress. Previous studies reported that PZT film orientation such as (111) depended on residual stress[47], where the (111) peak increased as the tensile stress increased. The analysis results of the XRD and Cross-section SEM images of the PLZST thin films indicate that the A-type thin film deposited on the $LaNiO_3$/Pt composite electrode exhibits a strong (100)-preferred orientation (blue curve) with a strong partner of (111) peak (see the **Fig. 1b)** and **Fig. 2e)**), while the B-type thin film exhibits a random orientation with a very weak (111) peak (see the **Fig. 1b)** and **Fig. 2g)**. Therefore, it seems reasonable to say that the decrease in (111) peak may be related to the degradation or relaxation of the in-plane residual tensile thermal stress when the thin film was deposited by the B-type mode. To unveil the case of the residual thermal stress in PLZST thin films, further investigations are made by the Raman spectra [48], the XRD $\sin^2\psi$ methods [45], and the strain mappings of the cross-sectional TEM images by using aberration-corrected high-angle annular dark-field (HAADF) Z-contrast STEM imaging [49]. As a result, the B-type thin film behaved as a FE rather than an AFE, and the *P-E* loops with a slight shrunk waist were obtained in the **Fig. 5g)** and **Fig. S6g)**. Therefore, it is believed that the *EC* effect in the PLZST thin film may be related to the amount of AFE phases and can be controlled by the distribution of the in-plane residual tensile thermal stress. The more the amount of the AFE phases, the larger the EC effect, as shown by the A-type thin film.

Moreover, the coexistence of multiple FE and AFE phases (**Fig. S4** and **Fig. 1a)**) are believed to be responsible for not only the dielectric relaxor dispersion but also the *EC* effect in a broad temperature range (the green vertical lines in **Fig. 5f)** and **5h)**). For practical applications, a large *EC* effect around room temperature is desired. One effective way to achieve this goal is doping with elements such as Sr and Ca, which not only can lower the temperature of the dielectric peak but also can stabilize the AFE phases [50].

Another feasible way is to shift the large *EC* effect to room temperature by modifying the composition of the thin film along the MPB line, as guided by the red arrows in **Fig. 1a)**. Combining the two ways is believed to realize a large *EC* effect near room temperature.

In practical applications, the maximum operating electric field is usually confined to the 1/3 of the safety applied electric field so that a large *EC* cooling sustainability can be ensured. In fact, it can be seen that the A-type thin film deposited on the $LaNiO_3$/Pt composite bottom electrode has exhibited a good *EC* cooling sustainability in a broad temperature range, as demonstrated by the well-developed $\varepsilon(E)$ and $\tan\delta(E)$ curves in **Fig. S4.** Where a large dc bias operating electric field is about 500 kV/cm, which is far higher than the 1/3 (364 $kVcm^{-1}$) of the *EC* safety applied electric field (1092 $kVcm^{-1}$).

Similar to the analysis of the *EC* effect, it is believed that the large pyroelectric energy harvesting performance in the A-type thin film deposited on the $LaNiO_3$/Pt composite electrodes is also related to the in-plane residual tensile thermal stress. All in all, it is believed that designing the composition near the MPB with two or multiple AFE phases coexisting, utilizing the metal/oxide composite electrode, and controlling the thermal stress are effective ways to make multi-functional ferroelectric materials with large *EC* effect and high pyroelectric energy density.

5. Conclusions

A large positive *EC* effect with $\Delta T > 10$K, and the maximum $\Delta T \sim 20.7$ K in a broad temperature range (about 110 K) was realized in PLZST relaxor antiferroelectric thin films. The in-plane residual thermal tensile stress during the layer-by-layer annealing process and the high quality film structure deposited on the $LaNiO_3$/Pt composite bottom electrode are responsible for the large EC effect. The great dielectric relaxor dispersion around the dielectric peak due to the coexistence of multiple FE and AFE phases results in the broad *EC* temperature range. Meanwhile, a large pyroelectric energy density (6.10 Jcm^{-3}) was also harvested by using an Olsen cycle. The large EC effect in a broad temperature range and high pyroelectric energy harvesting performance make the PLZST thin film an attractive multifunctional material for applications in

modern solid state cooling and energy harvesting.

Author Contributions

Biaolin Peng and Haitao Huang conceived the idea and designed the experiments. Biaolin Peng fabricated the samples and carried out most of the experiments. Biaolin Peng and Yinong Lyu carried out the TEM work. Biaolin Peng, Qi Zhang, and Haitao Huang wrote the paper. All the authors participated in the analysis and discussion of the results.

Additional information

Competing financial interests: The authors declare no competing financial interests.

References

[1] X. Moya, S. Kar-Narayan, N.D. Mathur, Nat. Mater. 13 (2014) 439-450.

[2] B. Neese, B.J. Chu, S.G. Lu, Y. Wang, E. Furman, Q.M. Zhang, Science 321 (2008) 821-823.

[3] A.S. Mischenko, Q. Zhang, J.F. Scott, R.W. Whatmore, N.D. Mathur, Science 311 (2006) 1270-1271.

[4] Y. Zhao, X.H. Hao, Q. Zhang, J. Mater. Chem. C 3 (2015) 1694-1699.

[5] S.P. Alpay, J. Mantese, S. Trolier-McKinstry, Q. Zhang, R.W. Whatmore, MRS Bull. 39 (2014) 1099-1111.

[6] H. Gu, X. Qian, X. Li, B. Craven, W. Zhu, A. Cheng, S.C. Yao, Q.M. Zhang, Appl. Phys. Lett. 102 (2013) 122904.

[7] X.-D. Jian, B. Lu, D.-D. Li, Y.-B. Yao, T. Tao, B. Liang, J.-H. Guo, Y.-J. Zeng, J.-L. Chen, S.-G. Lu, ACS Appl. Mat. Interfaces 10 (2018) 4801-4807.

[8] B. Lu, P. Li, Z. Tang, Y. Yao, X. Gao, W. Kleemann, S.-G. Lu, Scientific reports 7 (2017).

[9] R. Ma, Z. Zhang, K. Tong, D. Huber, R. Kornbluh, Y.S. Ju, Q. Pei, Science 357 (2017) 1130-1134.

[10] Q.M. Zhang, T. Zhang, Science 357 (2017) 1094-1095.

[11] B.L. Peng, H.Q. Fan, Q. Zhang, Adv. Funct. Mater. 23 (2013) 2987-2992.

[12] O. Tegus, E. Bruck, K.H.J. Buschow, F.R. de Boer, Nature 415 (2002) 150-152.

[13] B.A. Tuttle, D.A. Payne, Ferroelectrics 37 (1981) 603-606.

[14] M. Valant, Progress in Materials Science 57 (2012) 980-1009.

[15] W. Geng, Y. Liu, X. Meng, L. Bellaiche, J.F. Scott, B. Dkhil, A. Jiang, Adv Mater 27 (2015) 3165-3169.

[16] M. Ye, T. Li, Q. Sun, Z. Liu, B. Peng, C. Huang, P. Lin, S. Ke, X. Zeng, X. Peng, L. Chen, H. Huang, J. Mater. Chem. C 4 (2016) 3375-3378.

[17] M.H. Park, H.J. Kim, Y.J. Kim, T. Moon, K. Do Kim, Y.H. Lee, S.D. Hyun, C.S. Hwang, Advanced Materials 28 (2016) 7956-7961.

[18] R. Pirc, B. Rožič, J. Koruza, B. Malič, Z. Kutnjak, Europhys. Lett. 107 (2014) 17002.

[19] A.R. Akbarzadeh, S. Prosandeev, E.J. Walter, A. Al-Barakaty, L. Bellaiche, Phys Rev Lett 108 (2012) 257601.

[20] J. Íñiguez, M. Stengel, S. Prosandeev, L. Bellaiche, Physical Review B 90 (2014).

[21] I. Ponomareva, S. Lisenkov, Physical Review Letters 108 (2012).

[22] B. Li, J.B. Wang, X.L. Zhong, F. Wang, Y.K. Zeng, Y.C. Zhou, Epl 102 (2013).

[23] M. Ye, T. Li, Q. Sun, Z. Liu, B. Peng, C. Huang, P. Lin, S. Ke, X. Zeng, X. Peng, L. Chene, H. Huang, J. Mater. Chem. C 4 (2016) 3375-3378.

[24] F. Le Goupil, A.K. Axelsson, L.J. Dunne, M. Valant, G. Manos, T. Lukasiewicz, J. Dec, A. Berenov, N.M. Alford, Advanced Energy Materials 4 (2014).

[25] Y. Cai, F. Phillipp, A. Zimmermann, L. Zhou, F. Aldinger, M. Rühle, Acta Mater. 51 (2003) 6429-6436.

[26] B. Peng, Q. Zhang, X. Li, T. Sun, H. Fan, S. Ke, M. Ye, Y. Wang, W. Lu, H. Niu, X. Zeng, H. Huang, ACS Appl. Mat. Interfaces 7 (2015) 13512-13517.

[27] W.W. Jung, S.K. Choi, S.Y. Kweon, S.J. Yeom, Appl. Phys. Lett. 83 (2003) 2160.

[28] L. Pintilie, I. Boerasu, M. Gomes, M. Pereira, Thin Solid Films 458 (2004) 114-120.

[29] A.A. Bokov, Z.G. Ye, Appl. Phys. Lett. 77 (2000) 1888-1890.

[30] D. Fu, H. Taniguchi, M. Itoh, S.Y. Koshihara, N. Yamamoto, S. Mori, Phys Rev Lett 103 (2009) 207601.

[31] A.A. Bokov, Y.H. Bing, W. Chen, Z.G. Ye, S.A. Bogatina, I.P. Raevski, S.I. Raevskaya, E.V. Sahkar, Physical Review B 68 (2003).

[32] S. Ke, H. Fan, H. Huang, H.L.W. Chan, Appl. Phys. Lett. 93 (2008).

[33] S.G. Lu, Z.H. Cai, Y.X. Ouyang, Y.M. Deng, S.J. Zhang, Q.M. Zhang, Ceram. Int. 41 (2015) S15-S18.

[34] S.G. Lu, B. Rozic, Q.M. Zhang, Z. Kutnjak, R. Pirc, Applied Physics a-Materials Science & Processing 107 (2012) 559-566.

[35] T.K. Chin, F.Y. Lee, I.M. McKinley, S. Goljahi, C.S. Lynch, L. Pilon, IEEE Trans Ultrason Ferroelectr Freq Control 59 (2012) 2373-2385.

[36] X.L. Wang, X.H. Hao, Q.W. Zhang, S.L. An, X.J. Chou, Journal of Materials Science-Materials in Electronics 28 (2017) 1438-1448.

[37] H.R. Jo, C.S. Lynch, Smart Mater. Struct. 25 (2016).

[38] F.Y. Lee, H.R. Jo, C.S. Lynch, L. Pilon, Smart Mater. Struct. 22 (2013).

[39] T.K. Chin, F.Y. Lee, I.M. McKinley, S. Goljahi, C.S. Lynch, L. Pilon, Ieee Transactions on Ultrasonics Ferroelectrics and Frequency Control 59 (2012) 2373-2385.

[40] R. Kandilian, A. Navid, L. Pilon, Smart Materials & Structures 20 (2011).

[41] R.B. Olsen, D.A. Bruno, J.M. Briscoe, J. Appl. Phys. 58 (1985) 4709-4716.

[42] P. Liu, Z. Xu, X. Yao, Acta Physica Sinica 52 (2003) 2314-2318.

[43] A.V. Mazur, L.P. Stepanova, Mater. Sci. 41 (2005) 531-537.

[44] S. Corkovic, R.W. Whatmore, Q. Zhang, J. Appl. Phys. 103 (2008) 084101.

[45] B.H. Ma, S.S. Liu, S. Tong, M. Narayanan, R.E. Koritala, Z.Q. Hu, U. Balachandran, Smart Mater. Struct. 22 (2013).

[46] M.S. Mirshekarloo, K. Yao, T. Sritharan, Adv. Funct. Mater. 22 (2012) 4159-4164.

[47] H.X. Qin, J.S. Zhu, Z.Q. Jin, Y. Wang, Thin Solid Films 379 (2000) 72-75.

[48] J.H. Lee, K.S. Hwang, T.S. Kim, Appl. Phys. Lett. 96 (2010).

[49] Y.L. Tang, Y.L. Zhu, X.L. Ma, A.Y. Borisevich, A.N. Morozovska, E.A. Eliseev, W.Y. Wang, Y.J. Wang, Y.B. Xu, Z.D. Zhang, S.J. Pennycook, Science 348 (2015) 547-551.

[50] J.A. Rodriguez, A. Etxeberria, L. Gonzalez, A. Maiti, J. Chem. Phys. 117 (2002) 2699-2709.

Acknowledgements: This work was supported by the Research Grants Council of the Hong Kong Special Administrative Region, China (Project No. PolyU152665/16E), the National Natural Science Foundation of China (51402196), the Guangxi Science Foundation (Grants 2016GXNSFCB380006, 2017GXNSFFA198015), and the Scientific Research Foundation of Guangxi University (Grant XTZ160530).

Figure Captions:

Fig.1. (a) The phase diagram of the $Pb_{0.097}La_{0.02}(Zr,Sn,Ti)O_3$ system.[25] (b) XRD patterns of $Pb_{0.97}La_{0.02}(Zr_{0.65}Sn_{0.3}Ti_{0.05})O_3$ (PLZST) thin films with A-type and B-type annealing modes on Pt, $LaNiO_3$ and $LaNiO_3$/Pt bottom electrodes. FE: ferroelectric, AFE: antiferroelectric, T: tetragonal, O: orthorhombic, R: rhombohedral, HT: high temperature, LT: low temperature.

Fig.2. Cross-sectional and the corresponding surface SEM images of PLZST thin films. (a), (b) A-type on Pt electrode. (c), (d) A-type on $LaNiO_3$ electrode. (e), (f) A-type on $LaNiO_3$/Pt composite electrode. (g), (h) B-type on $LaNiO_3$/Pt composite electrode.

Fig.3. (a) Cross-sectional TEM image of the PLZST thin film with A-type annealing mode on $LaNiO_3$/Pt composite bottom electrode. Inset: magnified part of the thin film. (b) Cross-sectional HRTEM image of two adjacent laminar domains. Inset: the corresponding Fourier transform pattern. The blue or red dots in pairs: superlattice reflections.

Fig.4. $\varepsilon(T)$ and tan $\delta(T)$ of PLZST thin films: (a) A-type on Pt electrode, (b) A-type on $LaNiO_3$ electrode, (c) A-type on $LaNiO_3$/Pt composite electrode, and (d) B-type on $LaNiO_3$/Pt composite electrode.

Fig.5. *P*-*E* loops and the corresponding $\Delta T(T)$ of the PLZST thin films at selected temperatures. (a), (b) A-type on Pt electrode. (c), (d) A-type on $LaNiO_3$ electrode. (e), (f) A-type on $LaNiO_3$/Pt composite electrode. (g), (h) B-type on $LaNiO_3$/Pt composite electrode. Insets in (a), (c), (e) and (g): $P(T)$ (left upper corner) and $\partial P/\partial T$ (right lower corner) at selected electric fields. Insets in (b), (d), and the left upper corners of (f) and (h): $\Delta S(T)$. Insets in the right upper corners of (f) and (h): schematic diagrams of showing the in-plane thermally induced tensile stress (σ_t) in thin films.

Fig.6. Olsen cycle diagram of pyroelectric energy harvesting of the PLZST thin film on $LaNiO_3$/Pt composite electrode.

Fig.1:

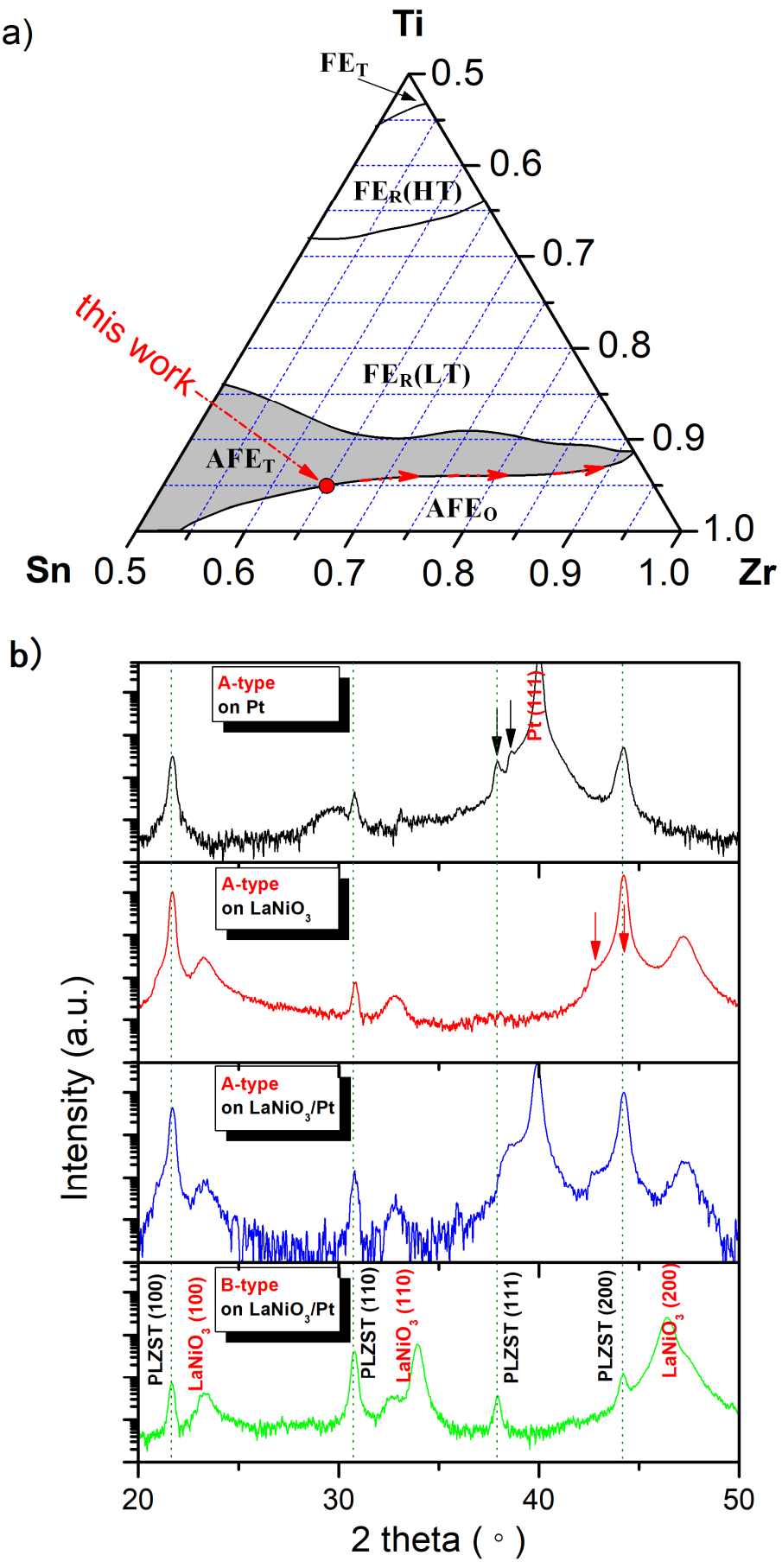
a)
Ti
FE$_T$
0.5
0.6
0.7
0.8
0.9
1.0
FE$_R$(HT)
FE$_R$(LT)
this work
AFE$_T$
AFE$_O$
Sn
Zr
b)
A-type
on Pt
Pt (111)
A-type
on LaNiO$_3$
A-type
on LaNiO$_3$/Pt
B-type
on LaNiO$_3$/Pt
PLZST (100)
LaNiO$_3$ (100)
PLZST (110)
LaNiO$_3$ (110)
PLZST (111)
PLZST (200)
LaNiO$_3$ (200)
Intensity (a.u.)
20
30
40
50
2 theta (◦)

Fig.2:

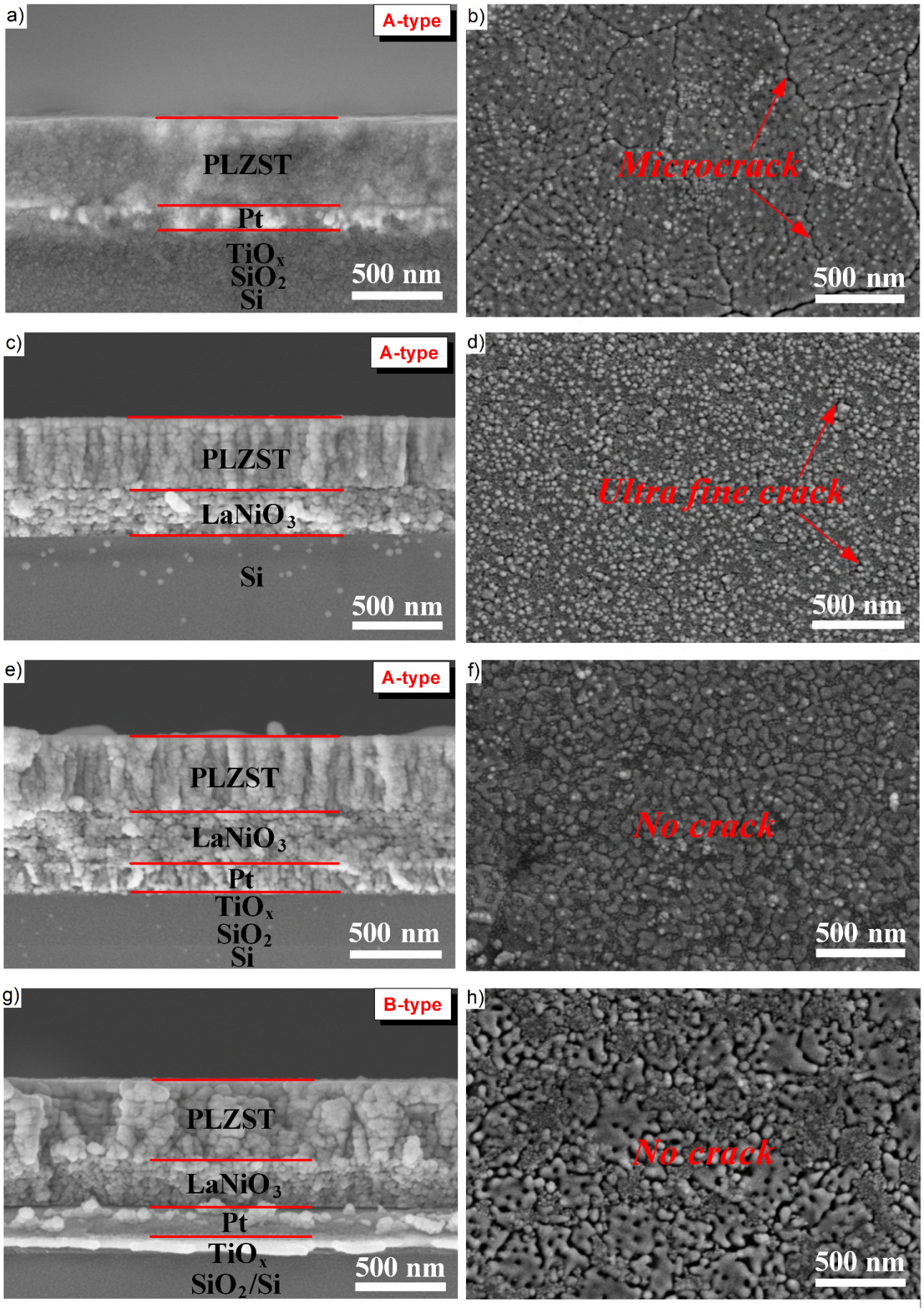
a)
A-type
PLZST
Pt
TiO_x
SiO_2
Si
500 nm
b)
Microcrack
500 nm
c)
A-type
PLZST
$LaNiO_3$
Si
500 nm
d)
Ultra fine crack
500 nm
e)
A-type
PLZST
$LaNiO_3$
Pt
TiO_x
SiO_2
Si
500 nm
f)
No crack
500 nm
g)
B-type
PLZST
$LaNiO_3$
Pt
TiO_x
SiO_2/Si
500 nm
h)
No crack
500 nm

Fig.3:

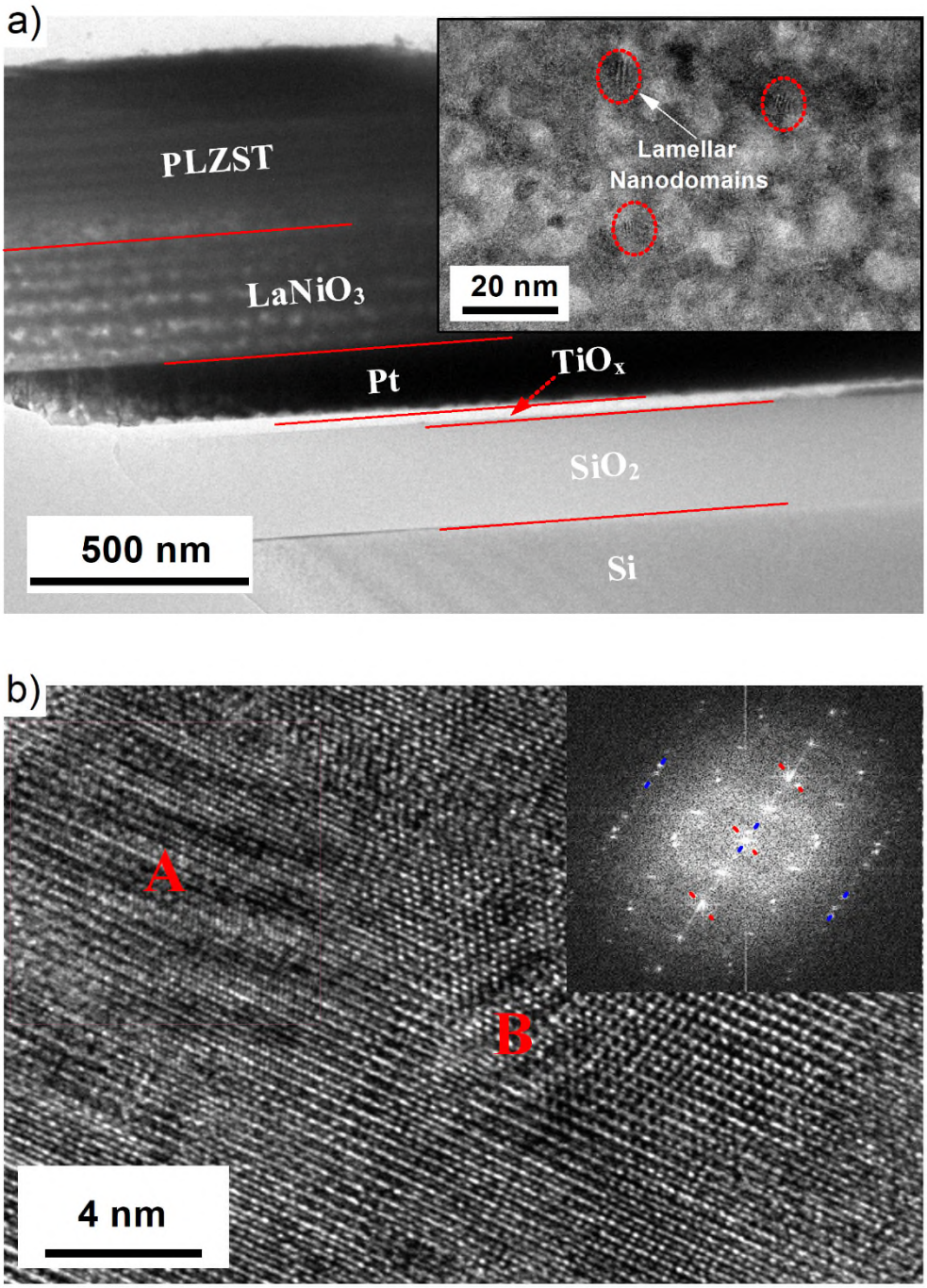
a)
PLZST
LaNiO3
Pt
TiOx
SiO2
Si
500 nm
Lamellar
Nanodomains
20 nm
b)
A
B
4 nm

Fig.4:

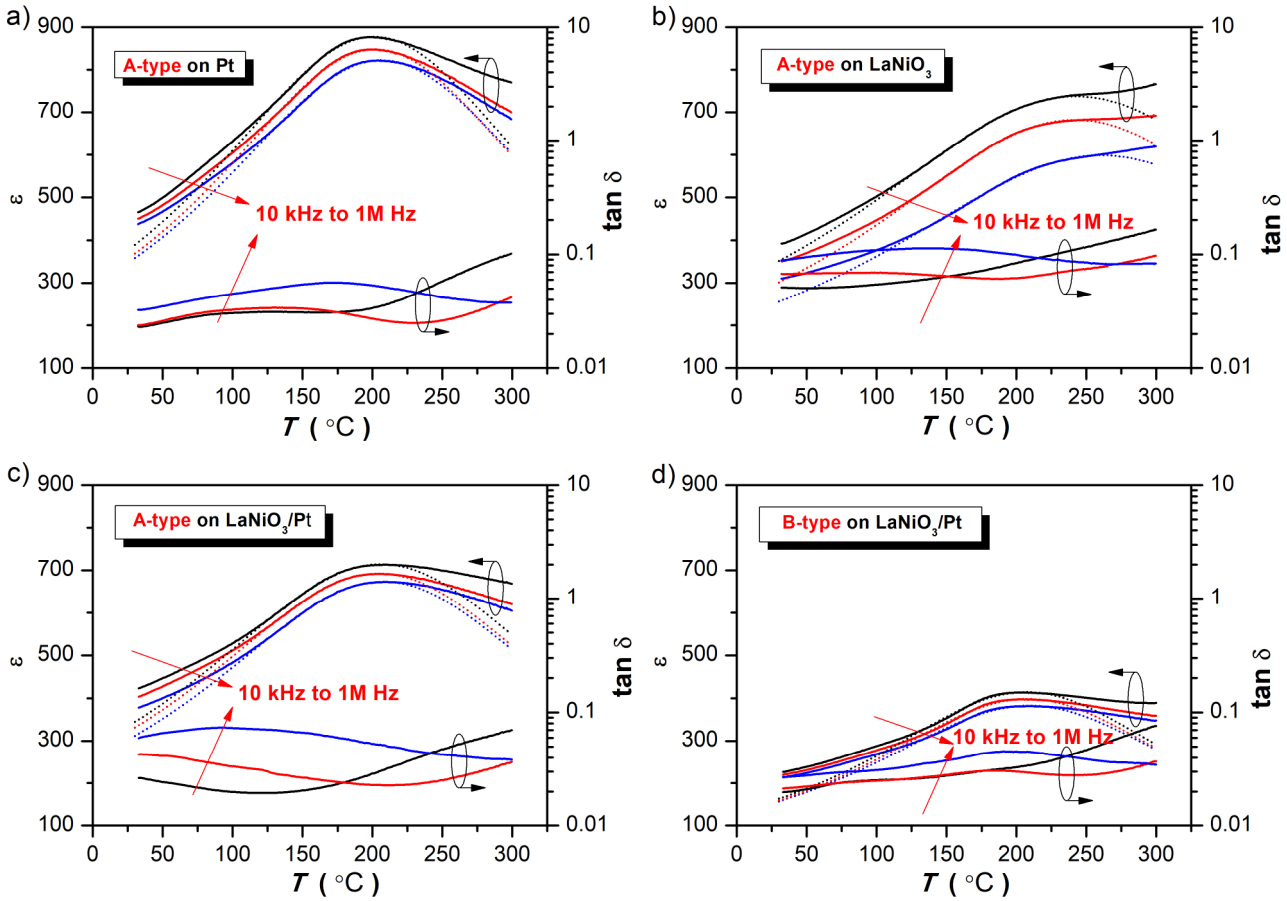
a)
A-type on Pt
10 kHz to 1M Hz
ε
tan δ
T (°C)
b)
A-type on LaNiO3
10 kHz to 1M Hz
ε
tan δ
T (°C)
c)
A-type on LaNiO3/Pt
10 kHz to 1M Hz
ε
tan δ
T (°C)
d)
B-type on LaNiO3/Pt
10 kHz to 1M Hz
ε
tan δ
T (°C)

Fig.5:

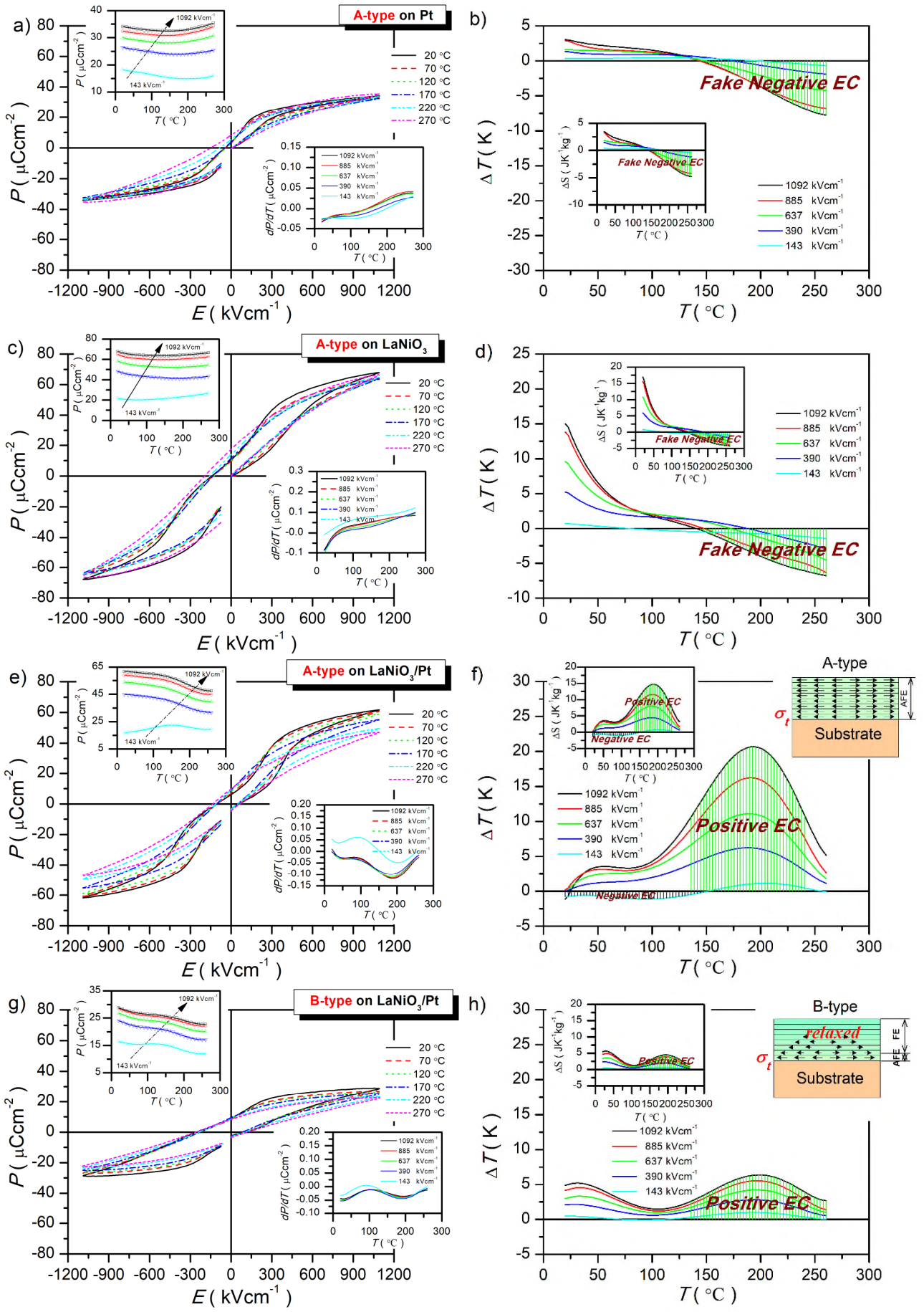
a)
A-type on Pt
20 °C
70 °C
120 °C
170 °C
220 °C
270 °C
1092 kVcm-1
143 kVcm-1
P (μCcm-2)
E (kVcm-1)
T (°C)
dP/dT (μCcm-2)
885 kVcm-1
637 kVcm-1
390 kVcm-1
b)
Fake Negative EC
ΔT (K)
ΔS (JK-1kg-1)
c)
A-type on LaNiO3
d)
e)
A-type on LaNiO3/Pt
f)
Positive EC
Negative EC
A-type
σt
AFE
Substrate
g)
B-type on LaNiO3/Pt
h)
B-type
relaxed
FE

Fig.6:

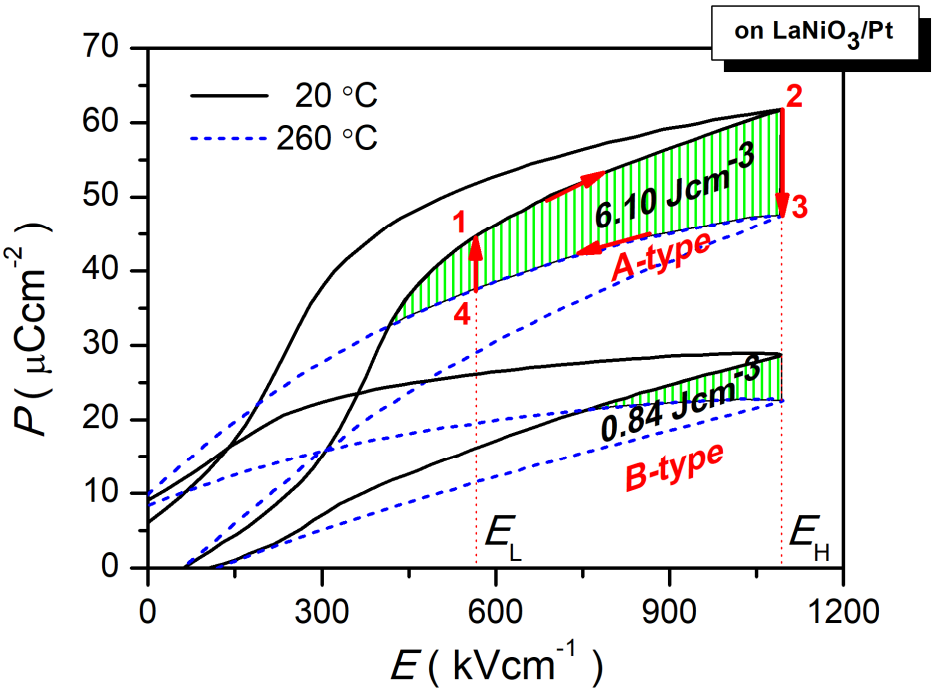
on LaNiO3/Pt
20 °C
260 °C
1
2
3
4
6.10 Jcm-3
A-type
0.84 Jcm-3
B-type
EL
EH
P (μCcm-2)
E (kVcm-1)
0
10
20
30
40
50
60
70
0
300
600
900
1200

Supplementary Materials for

Thermal strain induced large electrocaloric effect in a broad temperature range in nanoscale antiferroelectric and ferroelectric phases coexisting in a relaxor thin film on $LaNiO_3$/Pt composite electrode

Biaolin Peng[1,2,3], Qi Zhang[3], Yinong Lyu[2], Laijun Liu[2], Xiaojie Lou[4], Christopher Shaw[3], Haitao Huang[2]*, Zhonglin Wang[5]*

*Correspondence to: aphhuang@polyu.edu.hk; zhong.wang@mse.gatech.edu

This PDF file includes:

Figs. S1 to **S6**

Figure Captions:

Fig.S1. Flow charts of the sol-gel preparation and the spin coating process for (a) $Pb_{0.97}La_{0.02}(Zr_{0.65}Sn_{0.3}Ti_{0.05})O_3$ thin films using A-type or B-type annealing modes, and (b) $LaNiO_3$ bottom electrode.

Fig.S2. Color filtered optical microscope images of top electrodes on samples with (a) Pt bottom electrode and (b) $LaNiO_3$ or $LaNiO_3$/Pt composite bottom electrode.

Fig.S3. Schematic illustration of the four-point-probe resistivity measurement on (a) Pt, (b) $LaNiO_3$ and (c) $LaNiO_3$/Pt composite electrodes. (d) Electrical resistivity comparison chart of the three different types of bottom electrodes.

Fig.S4. Dc bias electric field dependence of the dielectric permittivity and dielectric loss of the PLZST thin film with A-type annealing mode on $LaNiO_3$/Pt composite electrode measured at different temperatures: (a) 30 °C, (b) 70 °C, (c) 110 °C, (d) 150 °C, (e) 190 °C, (f) 230 °C. AFE: antiferroelectric, FE: ferroelectric, T: tetragonal, O: orthorhombic, R: rhombohedral.

Fig.S5. Weibull distribution for the dielectric breakdown strength. Where n is the total number of samples, E_i is the breakdown electric field of the *i*th specimen arranged in ascending order ($E_1 \leq E_2 \leq E_{3...} \leq E_n$). The mean breakdown strength can be extracted from the point where the fitting line intersects with the horizontal axis at $\ln(\ln(1/(1-i/(n+1)))) = 0$.

Fig.S6. *P-E* loops and the corresponding *I-E* curves at selected electric fields. (a), (b) A-type on Pt electrode. (c), (d) A-type on $LaNiO_3$ electrode. (e), (f) A-type on $LaNiO_3$/Pt composite electrode. (g), (h) B-type on $LaNiO_3$/Pt composite electrode. The red *P-E* loops measured under the safety electric fields applied are far below than the mean dielectric breakdown strengths.

Fig.S1:

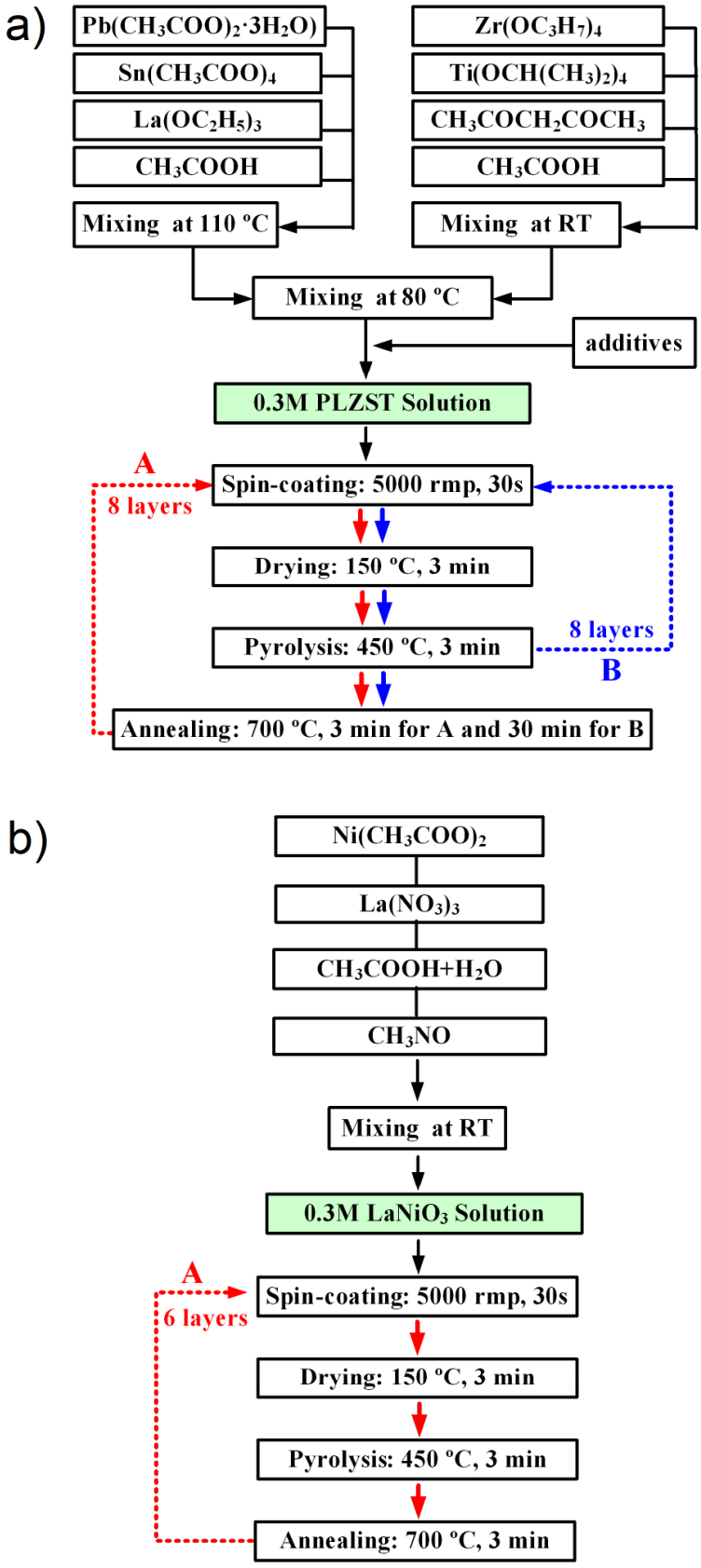
a)
Pb(CH3COO)2·3H2O)
Sn(CH3COO)4
La(OC2H5)3
CH3COOH
Mixing at 110 °C
Zr(OC3H7)4
Ti(OCH(CH3)2)4
CH3COCH2COCH3
CH3COOH
Mixing at RT
Mixing at 80 °C
additives
0.3M PLZST Solution
A
8 layers
Spin-coating: 5000 rmp, 30s
Drying: 150 °C, 3 min
Pyrolysis: 450 °C, 3 min
8 layers
B
Annealing: 700 °C, 3 min for A and 30 min for B
b)
Ni(CH3COO)2
La(NO3)3
CH3COOH+H2O
CH3NO
Mixing at RT
0.3M LaNiO3 Solution
A
6 layers
Spin-coating: 5000 rmp, 30s
Drying: 150 °C, 3 min
Pyrolysis: 450 °C, 3 min
Annealing: 700 °C, 3 min

Fig.S2:

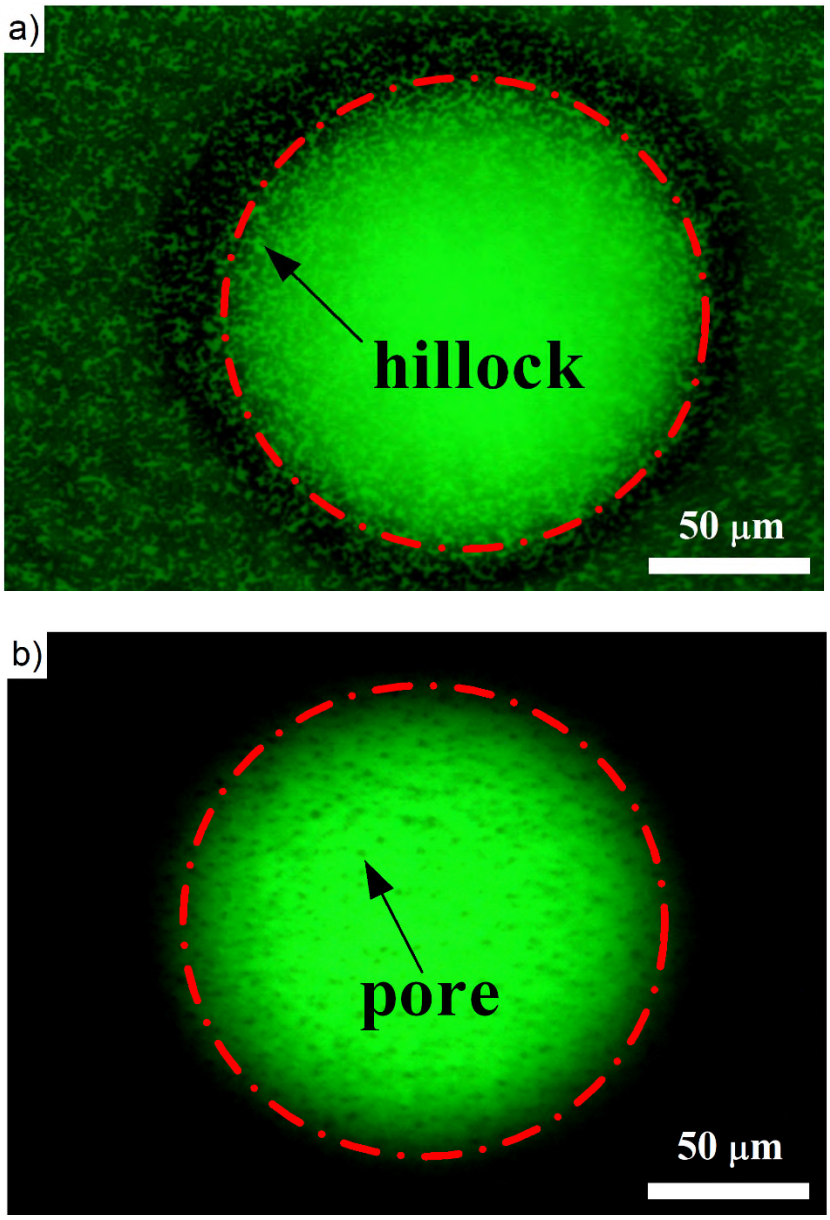

Fig.S3:

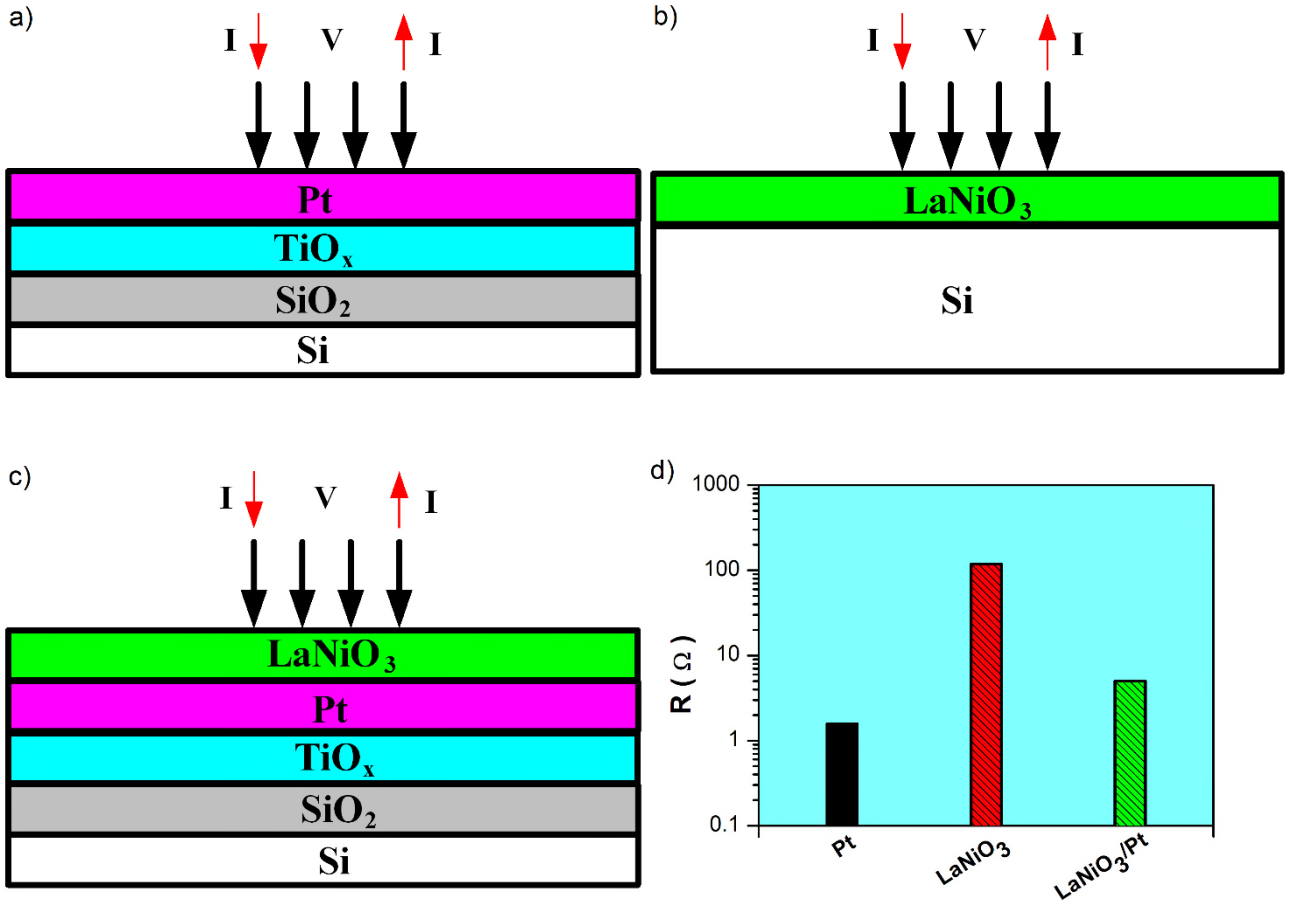
a)
I
V
I
Pt
TiOx
SiO2
Si
b)
I
V
I
LaNiO3
Si
c)
I
V
I
LaNiO3
Pt
TiOx
SiO2
Si
d)
1000
100
10
1
0.1
R (Ω)
Pt
LaNiO3
LaNiO3/Pt

Fig.S4:

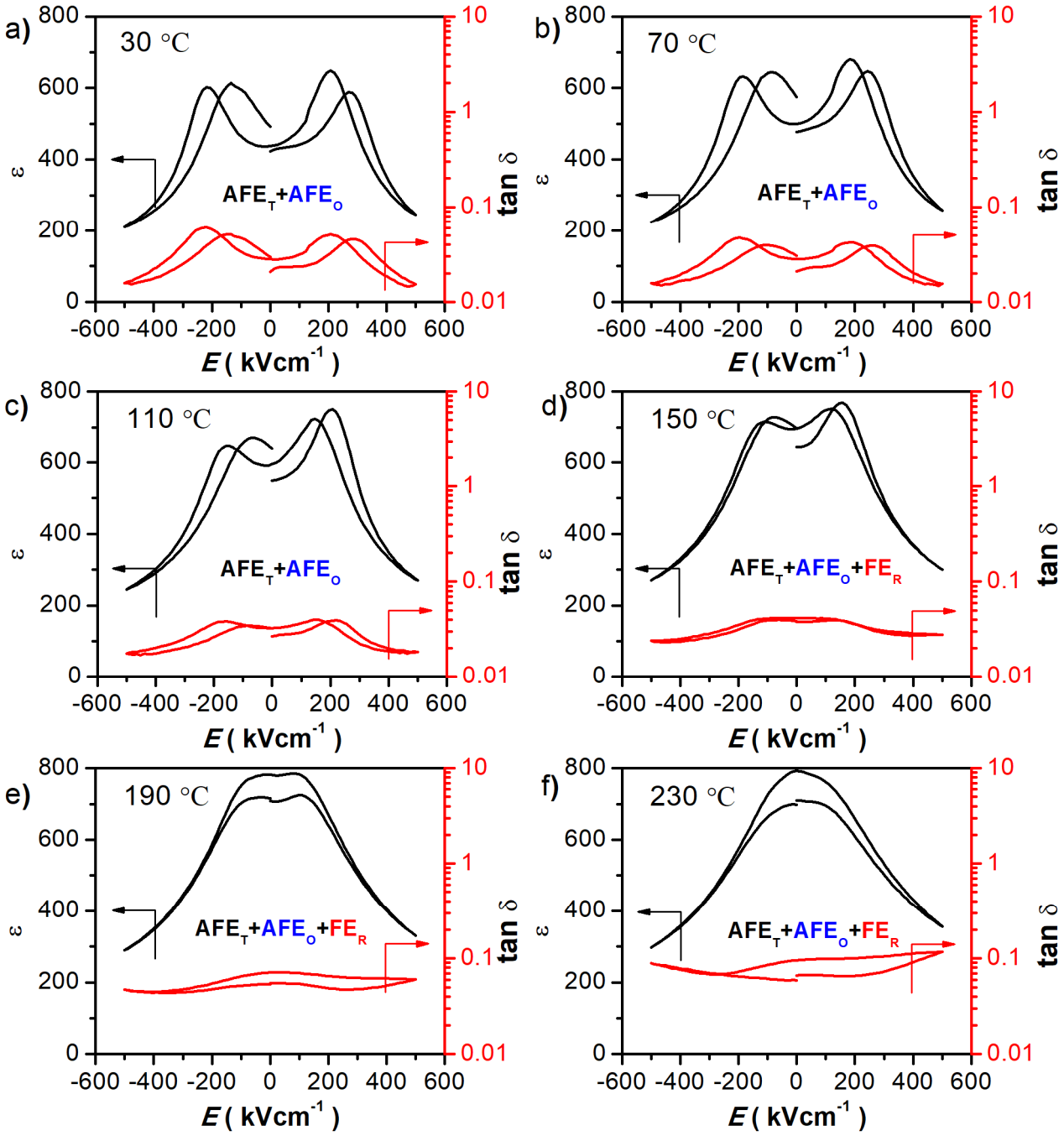
a)
30 °C
AFE$_T$+AFE$_O$
b)
70 °C
AFE$_T$+AFE$_O$
c)
110 °C
AFE$_T$+AFE$_O$
d)
150 °C
AFE$_T$+AFE$_O$+FE$_R$
e)
190 °C
AFE$_T$+AFE$_O$+FE$_R$
f)
230 °C
AFE$_T$+AFE$_O$+FE$_R$
ε
tan δ
E (kVcm^{-1})

Fig.S5:

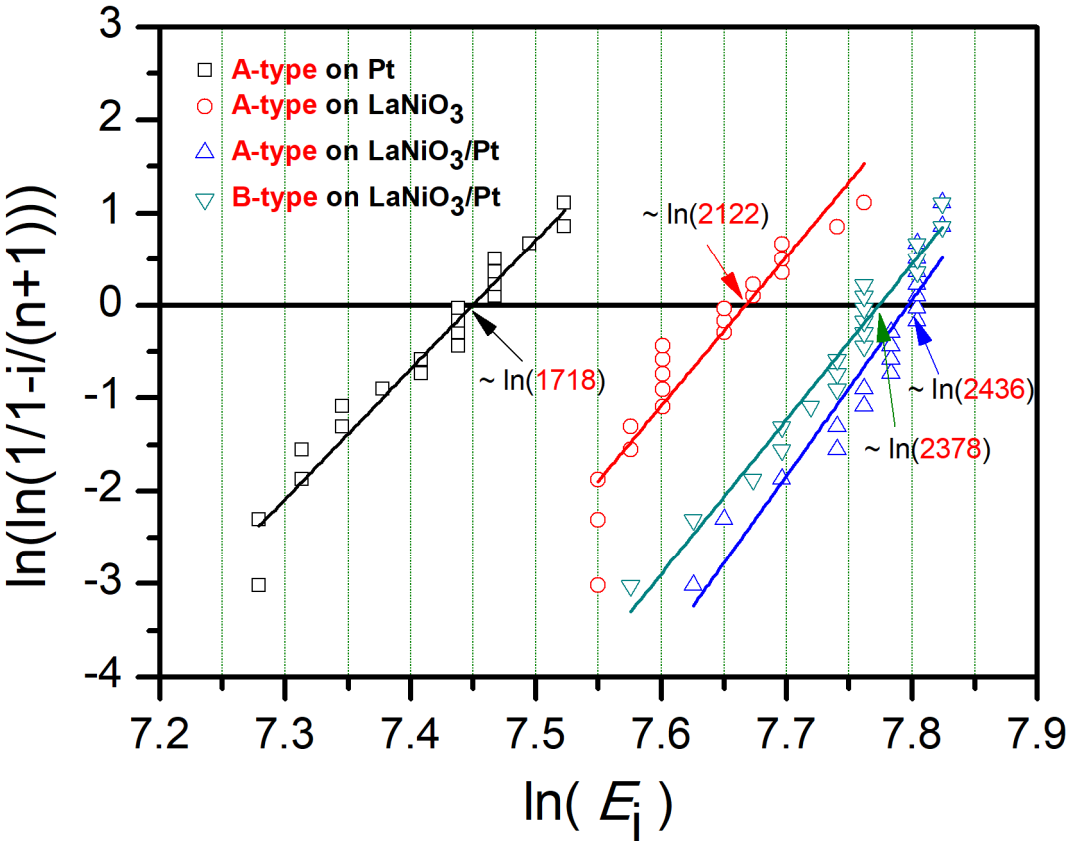
A-type on Pt
A-type on LaNiO3
A-type on LaNiO3/Pt
B-type on LaNiO3/Pt
~ ln(1718)
~ ln(2122)
~ ln(2378)
~ ln(2436)
ln(ln(1/1-i/(n+1)))
ln(Ei)
3
2
1
0
-1
-2
-3
-4
7.2
7.3
7.4
7.5
7.6
7.7
7.8
7.9

Fig.S6:

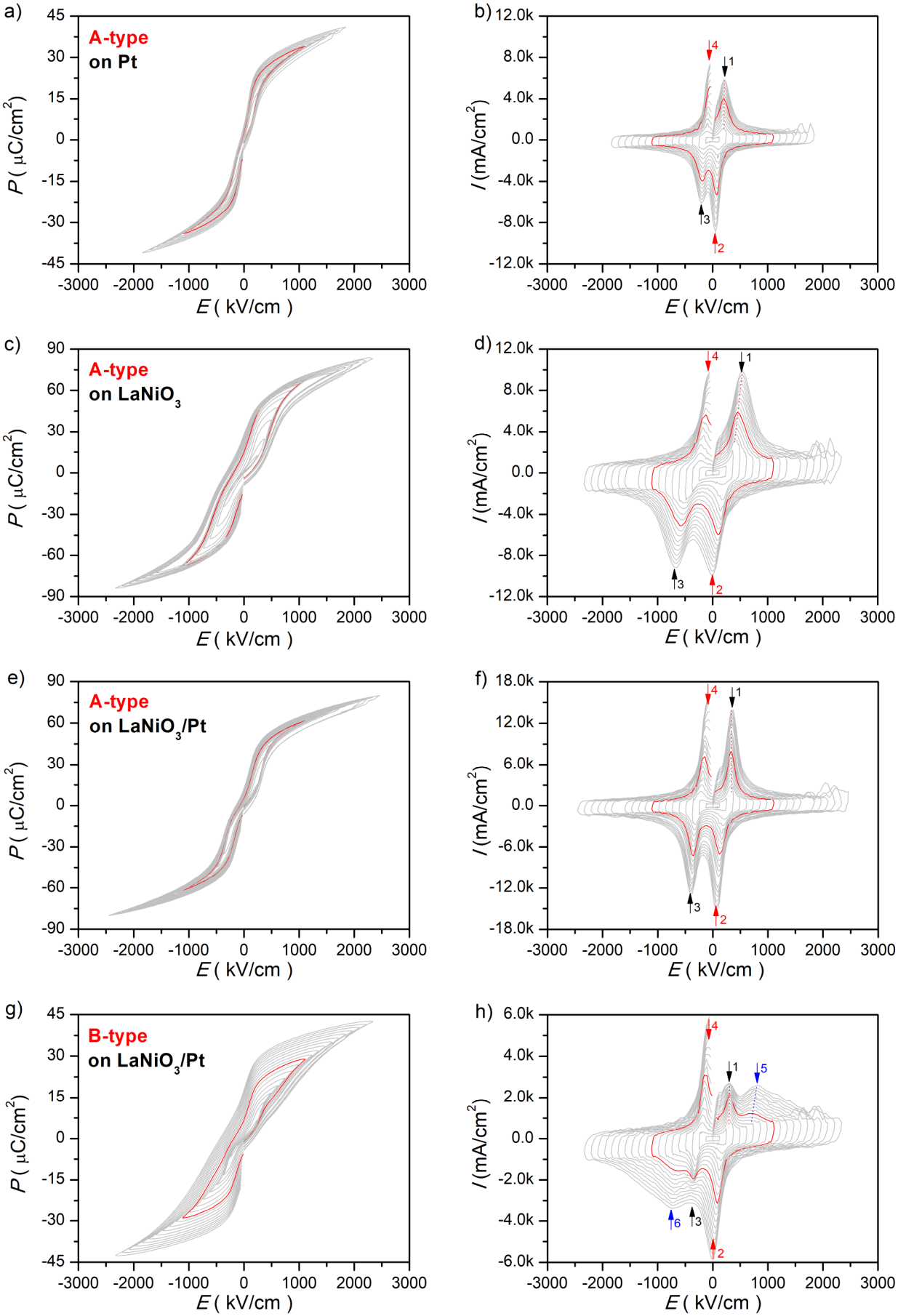
a)
A-type
on Pt
P (μC/cm2)
E (kV/cm)
b)
I (mA/cm2)
E (kV/cm)
c)
A-type
on LaNiO3
P (μC/cm2)
E (kV/cm)
d)
I (mA/cm2)
E (kV/cm)
e)
A-type
on LaNiO3/Pt
P (μC/cm2)
E (kV/cm)
f)
I (mA/cm2)
E (kV/cm)
g)
B-type
on LaNiO3/Pt
P (μC/cm2)
E (kV/cm)
h)
I (mA/cm2)
E (kV/cm)